Metals & corrosion

Microstructure and properties of CoCrFeNi-based multi-principal element alloys containing C and Sc

Mengwei He[1,2], Mehdi Eizadjou[1,2,*] ⓘ, Hansheng Chen[1,2], Hongwei Liu[1], Li Chang[2], and Simon P. Ringer[1,2,*] ⓘ

[1] *Australian Centre for Microscopy and Microanalysis, The University of Sydney, Sydney, NSW 2006, Australia*
[2] *School of Aerospace, Mechanical and Mechatronic Engineering, The University of Sydney, Sydney, NSW 2006, Australia*

ABSTRACT

A series of novel CoCrFeNi-based high-entropy alloys containing Sc and C were designed. These HEAs exhibited hardness, fracture toughness and wear resistance comparable or better than a range of selected benchmark systems. Microstructurally, we observed composite microstructures comprising variously a Sc-rich intermetallic phase, a sigma phase and an FCC solid solution phase within which precipitated $M_{23}C_6$ carbides. The Sc-rich intermetallic phase possessed a stoichiometry close to $(Co, M)_2(Sc, M)$, where M = Ni and Fe. As the carbon content increased, the hardness levels 'softened' from 799 VHN (C-free) to 674 VHN (C = 4 at.%), though the fracture toughness was increased $\sim 112\%$. At the same time, the specific wear rate was enhanced from 0.33×10^{-3} to 0.14×10^{-3} $mm^3 \cdot (N\ m)^{-1}$. The effectiveness of these microstructures in balancing high hardness, crack deflection and a relatively low wear rate was attributed to the enhanced stability of the FCC solid phase as the C content was increased.

GRAPHICAL ABSTRACT
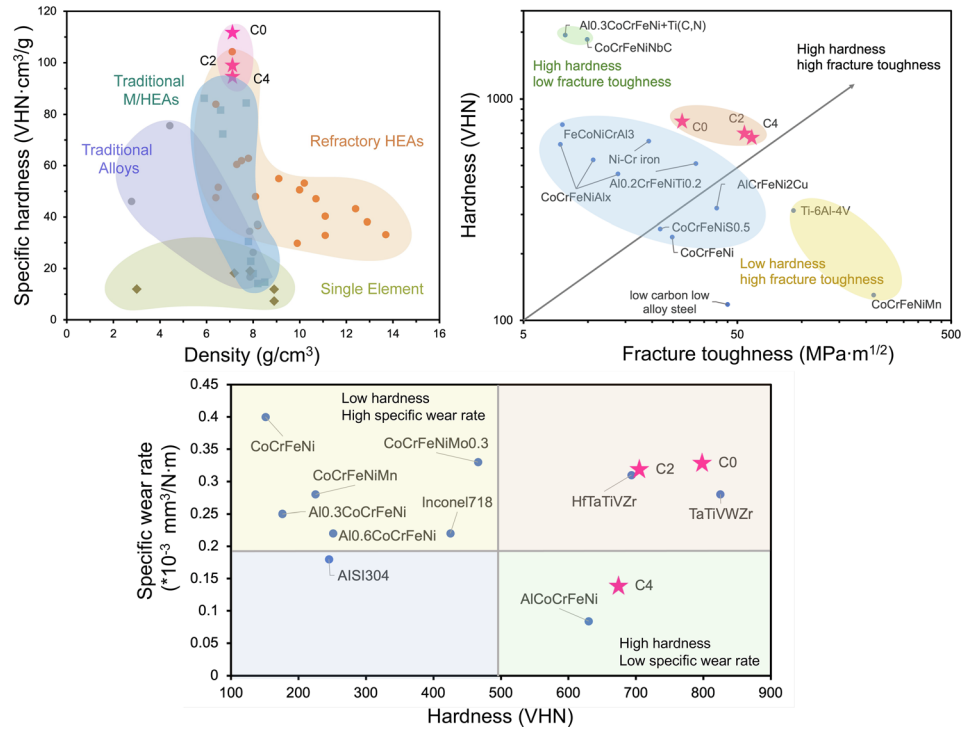
Introduction

High-entropy alloys (HEAs), also known as multi-principal element alloys (MPEA), have emerged as an exciting new class of materials [1, 2]. HEAs, especially CoCrFeNi-based HEAs, exhibit remarkable mechanical properties at room temperature and even better properties in the cryogenic regimes, as well as good wear resistance and other properties [3–8]. The majority of the research on HEAs has been focused on CoCrFeNi-based alloys and the addition of various fifth elements to investigate the potential for improved mechanical properties [3, 9]. For example, adding Mn, which has a small atomic mismatch, results in an equiatomic quinary CoCrFeNiMn alloy that preserves a single-phase face-centred cubic (FCC) structure with lattice parameter $a = 0.359$ nm [10] that exhibits remarkable fracture toughness, especially at cryogenic temperatures [4, 11, 12]. On the other hand, the addition of Nb, which has a large atomic misfit, leads to the formation of a ductile FCC

phase with lattice parameter $a = 0.3606$ nm (compared with $a = 0.3581$ nm in Nb free sample), and a second Nb-rich Laves intermetallic phase embedded in the FCC matrix [13]. These multi-phase HEAs have exceptional hardness and wear properties [14–16]. Jiang et al. [17] measured hardness and yield strength values of 515 VHN and 1745 MPa, respectively, in a CoCrFeNiNb HEA. However, as the hardness increases, the ductility and fracture toughness of the multi-phase HEAs decrease more rapidly that the diminishment observed in the single phase FCC CoCrFeNiMn alloys. Furthermore, both Mn and Nb are relatively heavy transition elements, which can be undesirable in structural materials.

The introduction of interstitial elements such as oxygen (O) [18], nitrogen (N) [19] and carbon (C) [20] has also been widely investigated. Of these, C is the most studied interstitial elemental addition to HEAs [21]. For example, Stepanov et al. [22] investigated the effects of the C content on the CoCrFeNiMn HEAs and revealed a 25% increase of the ultimate tensile strength

compared with similarly processed C-free HEAs. Wang et al. [23] demonstrated an increase in tensile elongation in a $Fe_{40.4}Ni_{11.3}Mn_{34.8}Al_{7.5}Cr_6$ HEA containing 1.1 at.% C compared to the C-free alloy. The addition of C has been shown to alter the phase stability and stacking fault energy of HEAs and has consistently demonstrated excellent potential to expand their structural properties [24, 25].

In this contribution, we have investigated the novel combination of scandium (Sc) as a substitutional element, in combination with C as an interstitial elemental addition to the familiar CoCrFeNi-based alloy. Sc was of particular interest as it has a large atomic radius but is one of the lighter transition metal elements and is widely associated with a strong interaction with vacancies as utilised in Sc-bearing Al-alloys gaining acceptance in the automobile and aerospace industries [26, 27].

Materials and methods

Materials processing and sample preparation

Three alloys of composition $(CoCrFeNiSc)_{100-x}C_x$ with C contents of $x = 0$, 2 and 4 at.% designated as alloys C0, C2 and C4, respectively, were prepared separately by arc melting. The raw materials were 99.99% purity cobalt (Co), iron (Fe), nickel (Ni), scandium (Sc), 99.5% purity chromium (Cr) and graphite (C) melted in an argon (Ar) atmosphere. Each alloy was remelted five times to improve homogeneity before being sectioned into smaller pieces using a diamond cutting wheel. Offcuts from each alloy were mechanically ground to 4000-grit sandpaper and polished to a mirror-like surface using successively finer diamond and silica suspensions, gradually down to a 0.25-μm silica suspension solution. Finally, the specimens were ion-milled using a Gatan PECS II system under 2 kV Ar ions.

Materials characterisation methods

X-ray diffraction (XRD) was performed using a PANalytical X'Pert Powder Cu source X-ray diffractometer between 30° and 90°. A Zeiss Ultra scanning electron microscope (SEM) with ancillary energy-dispersive X-ray spectroscopy (EDXS) and electron backscatter diffraction (EBSD) detectors was used to

investigate the microstructures. Hardness measurements were taken using a LECO Vickers Hardness Tester (LV700 AT) with a load of 3 kg and a dwell time of 15 s. The mean value of five indentations was used to report hardness values and associated errors [28]. The Vickers hardness indentations were also assessed using SEM to evaluate the indentation shapes and crack lengths. Values for the fracture toughness (K_{IC}) of these samples were then estimated based on the Palmqvist method for the estimation of toughness using the length of the cracks formed by the hardness indenter by applying the following formulae [29–31]:

$$K_{IC} = 0.0028 \times \sqrt{1000 \times H \times g^2 \times \frac{M}{L_{Tol}}} \qquad (1)$$

$$L_{Tol} = L1 + L2 + L3 + L4 \qquad (2)$$

where H is the hardness (VHN), L_{Tol} is the sum of crack lengths from the corner of indentation expressed as mm, M is the applied load (kg), and g is the acceleration due to gravity (9.81 m s^{-2}).

A ball-on-disc sliding method was used on a commercial tribometer (NANOVEA-MT/60/NI) to assess the wear resistance of these alloys. Tungsten carbide balls with a radius of 2.38 mm were used, and each test was carried out under 20 N for 30 min with a sliding speed of 0.05 m s^{-1} in air at room temperature. The specific wear rate was calculated according to Eq. (3):

$$W_s = \frac{\Delta m}{\rho \times F_N \times L} \qquad (3)$$

where W_s corresponds to the specific wear rate ($\frac{mm^3}{N \times m}$), Δm is the weight loss after the test (g), ρ is the density of the material (g·mm^{-3}), F_N is the force applied on the sample (N), and L is the sliding length (m). Transmission electron microscopy was conducted using a JEOL 2200 TEM, operating at an accelerating voltage of 200 kV. Atom probe tomography (APT) was conducted using CAMECA LEAP3000Si operating in voltage mode at 50 K, 20% pulse fraction, 200 kHz pulse rate and evaporation rate of 0.2 [32]. Specimens for TEM and APT were prepared using standard techniques.

Results and discussion

Mechanical properties

Figure 1a charts values for the specific hardness ($\frac{hardness(VHN)}{density(\frac{g}{cm^3})}$) of the C0, C2 and C4 alloys and provides
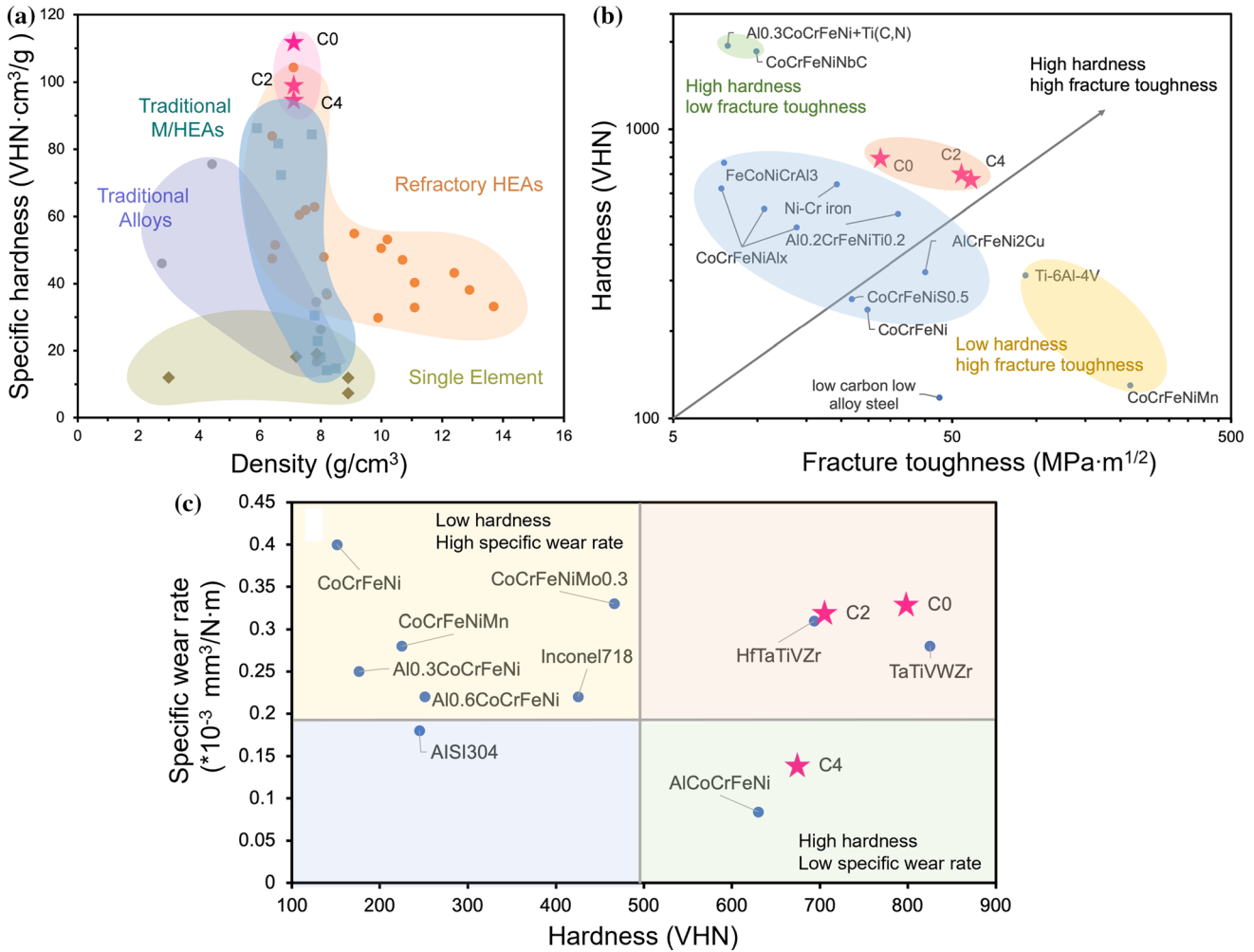
Figure 1 Mechanical properties of the experimental CrNiFeCoSc-C alloys introduced here compared to other relevant alloy systems. **a** Specific hardness versus density; **b** hardness versus fracture toughness (log–log scale); and **c** specific wear rate versus hardness.

a comparison to values for the relevant individual elements, binary alloys, the CoCrNi-based ternary and Fe-bearing quaternary HEAs, and certain refractory HEAs taken from the literature [33–42]. The specific hardness of all three alloys C0, C2 and C4 was higher than the binary alloys and the other HEAs possessing similar densities. The specific hardness values were almost 1.5 times larger than Ti–6Al–4V (75 VHN cm^3 g^{-1}), ~ 5 times greater than the single phase FCC CoCrFeNiMn (22 VNH cm^3 g^{-1}) and ~ 6 times greater than the CoCrFeNi base alloy (18 VNH cm^3 g^{-1}). Figure 1b summarises the estimates of the fracture toughness of these alloys in comparison to values from the literature of other major HEAs and relevant alloys [43–51] using different methods. The C0 alloy exhibits a hardness of 799 VHN and a fracture toughness of 27.6 MPa m$^{1/2}$. The C-bearing alloys exhibit lower hardness but

higher apparent fracture toughness. Alloy C2 possessed a hardness of 705 VHN, and our estimate of the fracture toughness was almost twice that of the alloy C0, reaching 54.0 MPa m$^{1/2}$. At 4 at.% C, the hardness decreased by 4% compared to C2, while the fracture toughness increased a further 8%. The hardness of alloy C4 was ~ 15% lower than alloy C0, and the fracture toughness was ~ 112% higher. Figure 1c presents the specific wear rates of the HEAs introduced here compared to other relevant alloys [52–55]. The specific wear rates of the alloys C0, C2 and C4 were 0.33 × 10^{-3}, 0.32 × 10^{-3} and 0.14 × 10^{-3} mm^3·(N·m)$^{-1}$, respectively. This is better than the specific wear rate of the CoCrFeNi alloy (0.4 × 10^{-3} mm^3·(N·m)$^{-1}$). The average friction coefficient of these alloys ranged between 0.65 and 0.74. The wear resistance trended in direct proportionality with the apparent fracture toughness such

that alloy C4 exhibited the highest fracture toughness and outstanding wear resistance. Here, we point out that the literature cited in our compilations in Fig. 1 contains the details of the measurement techniques variously used to assess the wear resistance, hardness and fracture toughness. The techniques were not identical, and we acknowledge that there is some potential for technique-dependent variations between the studies compiled. In the absence of unitary standard measurements for these values, we have carefully selected the studies for these compilations both to summarise the state of the art and to provide guidance in terms of how our measurements benchmark to similar systems.

The relationship between microstructure and mechanical properties

The XRD spectrum (supplementary) identified the presence of the FCC matrix phase commonly reported in CoCrFeNi HEAs (Fd$\overline{3}$m, $a = 0.358$ nm) [13], an intermetallic (IM) phase with a Co$_2$Sc type cubic structure (Fd$\overline{3}$m, $a = 0.690$ nm) and a tetragonal Fe$_{1.01}$Cr$_{0.99}$ type sigma phase (P4$_2$/mnm, $a = 0.878$, $c = 0.456$ nm) in the C0 alloy [56]. Additional peaks for the FCC M$_{23}$C$_6$ carbide phase (Fm$\overline{3}$m, $a = 1.059$ nm) [57] were detected in both the C2 and C4 alloys. With increasing C content, the lattice parameter of the FCC solid solution phase increased $\sim 0.5\%$ from 0.357 to 0.359 nm, and the peaks from the sigma phase diminished in height indicating a reduction of its phase fraction.

Figure 2 provides the EBSD and EDXS of the three HEAs. The data in Fig. 2a–c confirm that C effectively reduced the phase fraction of the sigma phase in this system from 35.4% in alloy C0 to 6.3% in alloy C2 and $\sim 0.1\%$. Figure 2 further reveals that the IM phase fraction was increased from 41.2% (C0) to 54.0% (C2) and then unchanged from C2 to C4. In terms of the FCC phase, Fig. 2 reveals that, from C0 to C2, the phase fraction of the FCC phase increased from 18.9 to 26.8%.

The hardness trends observed in these experimental alloys, where we report an 11% softening from alloy C0 (799 VHN) to C2 (705 VHN) and a further 4% softening from alloy C2 to C4 (674 VHN), are attributed mainly to the increased stability of the relatively soft FCC phase, which replaced the significantly harder sigma phase. Based on other reports

[58], the hardness of the sigma phase is ~ 957 VHN and the M$_{23}$C$_6$ carbide phase is ~ 1250 VHN. On the other hand, the hardness of the FCC phase has been reported as ~ 120 VHN [59] and it can also be expected to be relatively ductile. The compositing of the hardness is overall significant, and we note that the occurrence of the very hard M$_{23}$C$_6$ carbide phases within the softer FCC matrix. This results in a situation whereby, notwithstanding the significant increase in the phase fraction of the softer FCC phase, the overall hardness changes by only $\sim 16\%$ overall between the three alloys.

Although the addition of the C led to microstructural changes that affected only a minor softening of the alloys, these changes brought about a significant increase the fracture toughness (Fig. 2a–c.) In the C0 sample, as shown in Fig. 2a, we observed a coarse lamellar microstructure comprised of the IM phase and the sigma phase with residual FCC phase occurring at the sigma-IM phase interfaces. The introduction of C to the level of 2 at.%, as shown in Fig. 2b, brings about a blocky-type microstructure and the IM phase is now enveloped by the FCC phase which also contains M$_{23}$C$_6$ carbide precipitation. Figure 2c provides the EBSD map for the alloy containing 4 at.% C, and it is dominated by coarse lamella of the IM phase in the FCC phase, with M$_{23}$C$_6$ carbide precipitation evident in the FCC solid solution phase.

Figure 2d provides an SEM image of a crack emanating from the corner of a hardness indent in the sample C4 and reveals that the crack prefers to propagate through the IM phase. The length of these cracks was used to estimate of the fracture toughness as described above. We found that the mean crack length in the C0 samples was 59.31 μm and this value decreased sharply by 77% to 13.67 μm after the introduction of 2 at.% C. We suggest that the microstructure is a key factor in the improvement of the fracture toughness here, as has also been reported in other systems [60]. In alloy C0 (Fig. 2a), the IM phase occurs as coarse globules and is in direct contact with the sigma phase throughout. The occurrence of these two intermetallic phases in direct contact appears to offer an easy crack pathway and consequently, lower fracture toughness. The addition of 2 at.% C (Fig. 2b) and the associated replacement of the brittle sigma phase by the more ductile FCC solid solution phase that contains a dispersion of M$_{23}$C$_6$ carbides results in an inhibition of the crack

**FCC**   **IM**   **Sigma**   **M$_{23}$C$_6$**
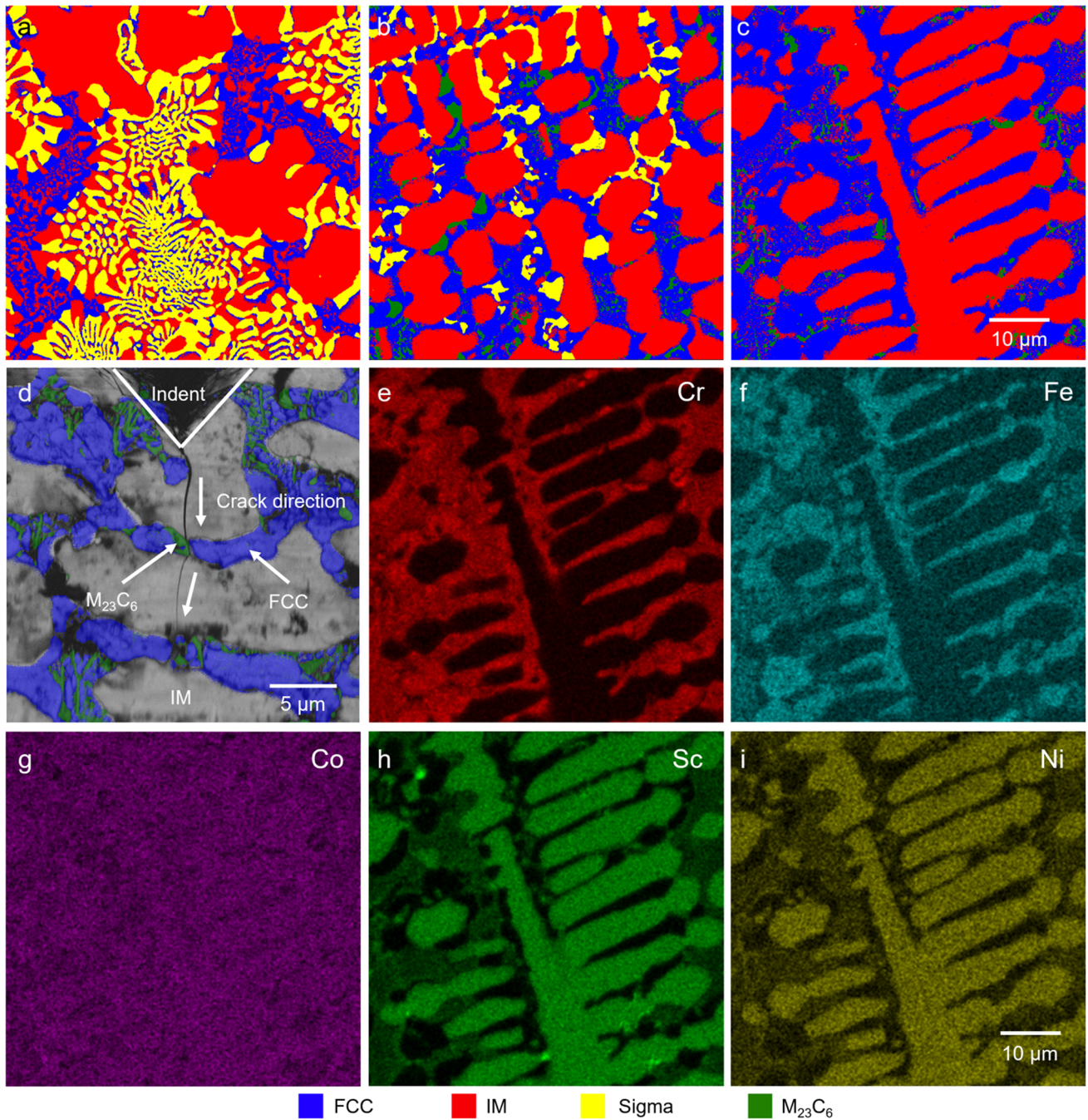
Figure 2 SEM-based imaging from the alloys investigated. **a–d** are EBSD maps, as follows: **a** CrNiFeCoSc-based alloy (C0), **b** CrNiFeCoSc-2 at.%C alloy (C2), **c** CrNiFeCoSc-4 at.%C alloy (C4), **d** crack propagation in alloy C4. **e–i** are EDXS maps from sample C4 as follows: **e** Cr, **f** Fe, **g** Co, **h** Sc and **i** Ni.

propagation. This was also the case in alloy C4 (Fig. 2c–d), and it is apparent that the FCC phase changes the direction of crack propagation, especially where exists precipitation of M$_{23}$C$_6$ carbide. The result is a further reduction of the extension of the crack (Fig. 2d). As indicated from the XRD data, the addition of C slightly distorted the FCC crystal

lattice, which appears to have increased the amount of plastic deformation required to propagate the crack [61]. Correlative EDXS maps were also recorded from the alloy C4 (Fig. 2f–i). The FCC solid solution was observed to be enriched in Cr and Fe, the M$_{23}$C$_6$ carbides were enriched in Cr, while the Sc rich IM phase was enriched with significant Co and
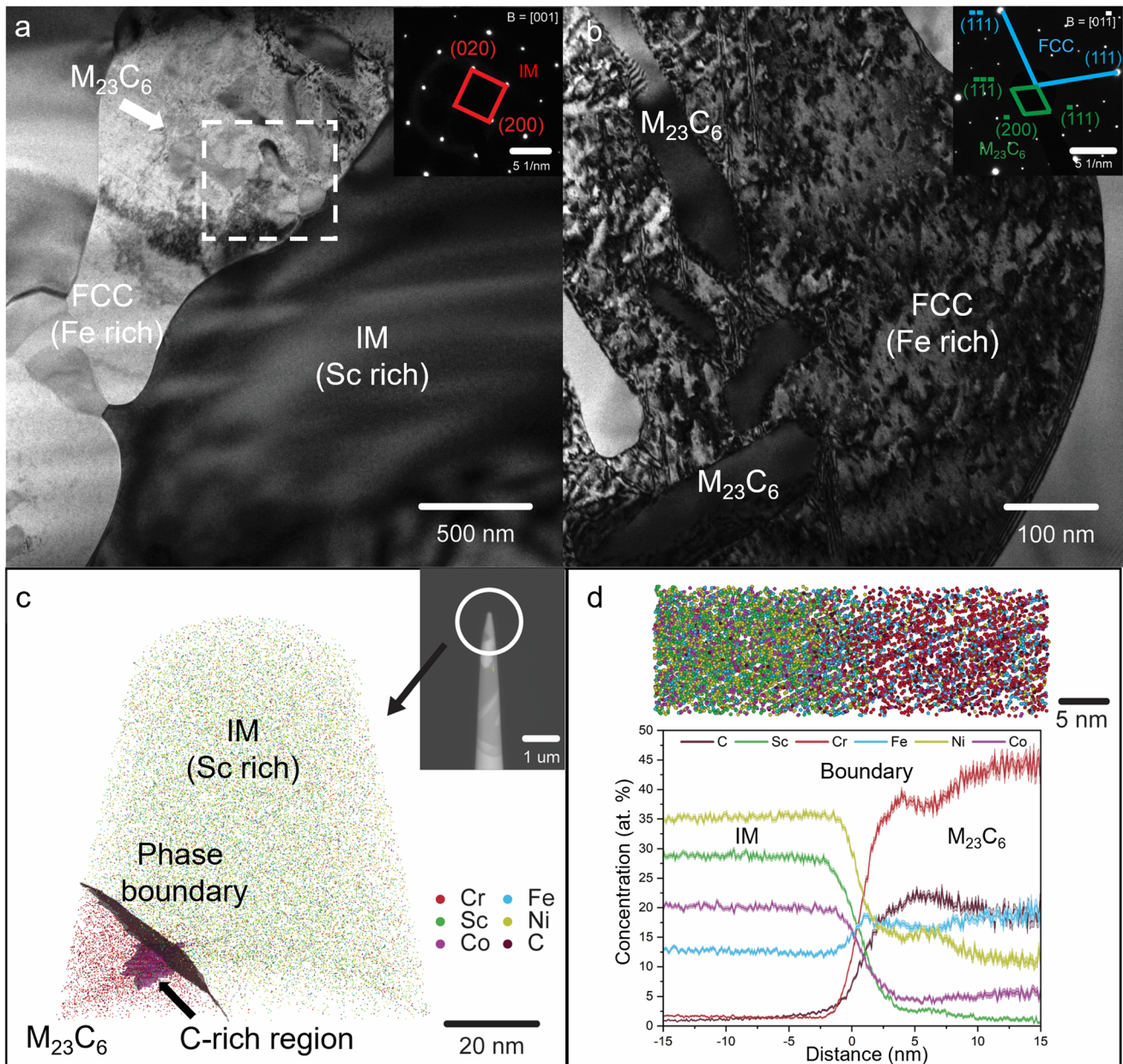
Figure 3 TEM and APT analysis of alloy C4. **a** and **b** TEM bright-field images with inset SAED patterns of the Sc-rich IM, the Fe-rich FCC solid solution phase and the $M_{23}C_6$ carbide phases. Some dislocation debris remains in the FCC phase. **c** APT atom map of an interface between the Sc-rich IM phase and the $M_{23}C_6$ phase. An SEM image of the corresponding APT tip is inset. **d** Atom map and the element concentration profile across the phase boundary in (**c**). The concentration profiles for each element are plotted as the trace of the mean with the standard error shaded.

Ni. Thermodynamic calculations of the effect of C-additions to CoCrFeNi-based [62] HEAs indicate that both FCC and $M_{23}C_6$ carbide can form at temperatures $\sim 1000\,^\circ C$, whereas the sigma phase is formed between ~ 500 and $\sim 800\,^\circ C$ [63]. In our current study, 2 at.% carbon enabled equilibrium between both the FCC phase and the $M_{23}C_6$ phase and we suggest that the sigma phase precipitated

during the cooling process. Interestingly, the co-existence of these phases has also been studied in Cr-bearing steels [64]. From our EDXS results, both the carbide and sigma phases were Cr rich. The thermodynamic and kinetic pre-requisites for the formation of $M_{23}C_6$ carbide and sigma phase are such that the volume fraction of both of these phases was reduced, which resulted in enhanced FCC stability.

TEM and APT analyses were conducted on alloy C4 to better understand this microstructure. As is evident in the TEM images provided in Fig. 3a–b, the Cr-rich $M_{23}C_6$ precipitation that occurred in the FCC solid solution phase possessed an ellipsoidal morphology. The TEM images indicate that these carbides were between 100 and 300 nm in their longest dimension. The SAED pattern inset in Fig. 3b indicates that the FCC phase and $M_{23}C_6$ carbide exhibit orientation relationships such that $\{111\}_{FCC}//\{111\}_{M23C6}$ and $<01\bar{1}>_{FCC}//<01\bar{1}>_{M23C6}$. An APT analysis at the interface between the Sc-rich IM phase and an $M_{23}C_6$ carbide is provided in Fig. 3c–d. The carbide appears enriched in both Cr and Fe, and there is some evidence of a C-rich region at the phase boundary. We have used this analysis to estimate the Sc-rich IM phase as comprising 28.7 at.% Sc, 35.3 at.% Ni, 20.2 at.% Co, and 12.7 at.% Fe suggestive of a $(Co, M)_2(Sc, M)$ stoichiometry, where M = Ni and Fe. Strengthening/hardening from carbide precipitation as well as changes to the phase fractions are put forward as the critical factors that explain the simultaneous reduction in hardness and increase fracture toughness with increasing C content. The fact that $M_{23}C_6$ carbide formed instead of the sigma phase is demonstrated in Fig. 2a, b. Both phases are hard but brittle. The overall fraction of these phases reduced with increasing FCC phase fraction. For example, the more local observations in Fig. 2d, Fig. 3b, d, the embedded hard $M_{23}C_6$ carbides were dispersed in the relative soft FCC phase. This seems to achieve a desirable balance in hardness and fracture toughness.

The changes in the type and distribution of the microstructural phases also contributed to changes in the measured wear resistance. Compared to the CoCrFeNi-based alloy, where the microstructure was dominated by the sigma phase, the specific wear rate of the C4 alloy decreased $\sim 65\%$. From the Sc-bearing alloy C0 to the Sc + C-bearing alloy C4, the specific wear rate decreased more than 50%. The replacement of the sigma phase by the carbides within the FCC phases played a key role as does the toughness of the Sc-bearing IM phase.

Conclusions

In summary, we have measured the hardness, fracture toughness and the specific wear rate of a novel series of CoCrFeNi HEAs to which Sc and C were added. The new Sc- and C-bearing HEAs not only maintained high hardness, but also exhibited higher fracture toughness and improved wear resistance than many comparable systems.

Microstructurally, we observed a Sc-rich intermetallic phase of approximate composition 28.7 at.% Sc, 35.3 at.% Ni, 20.2 at.% Co, and 12.7 at.% Fe, and a FCC solid solution phase within which occurred $M_{23}C_6$ carbides, which was effective at supporting high hardness, deflecting cracks and a low wear rate.

Declarations

Conflict of interest The authors declare that they have no conflict of interest.

Supplementary Information: The online version contains supplementary material available at https://doi.org/10.1007/s10853-022-07227-3.

References

[1] Yeh J-W, Chen S-K, Lin S-J et al (2004) Nanostructured high-entropy alloys with multiple principal elements: novel alloy design concepts and outcomes. Adv Eng Mater 6(5):299–303. https://doi.org/10.1002/adem.200300567

[2] Cantor B (2014) Multicomponent and high entropy alloys. Entropy 16(9):4749–4768. https://doi.org/10.3390/e16094749

[3] George EP, Raabe D, Ritchie RO (2019) High-entropy alloys. Nat Rev Mater 4(8):515–534. https://doi.org/10.1038/s41578-019-0121-4

[4] Gludovatz B, Hohenwarter A, Catoor D, Chang EH, George EP, Ritchie RO (2014) A fracture-resistant high-entropy alloy for cryogenic applications. Science 345(6201):1153–1158. https://doi.org/10.1126/science.1254581

[5] Gludovatz B, Hohenwarter A, Thurston KVS, Bei H, Wu Z, George EP, Ritchie RO (2016) Exceptional damage-tolerance of a medium-entropy alloy CrCoNi at cryogenic temperatures. Nat Commun 7(1):10602. https://doi.org/10.1038/ncomms10602

[6] Laplanche G, Kostka A, Reinhart C, Hunfeld J, Eggeler G, George EP (2017) Reasons for the superior mechanical properties of medium-entropy CrCoNi compared to high-entropy CrMnFeCoNi. Acta Mater 128:292–303. https://doi.org/10.1016/j.actamat.2017.02.036

[7] Wang M, Lu Y, Zhang G, Cui H, Xu D, Wei N, Li T (2021) A novel high-entropy alloy composite coating with core-shell structures prepared by plasma cladding. Vacuu 184:109905. https://doi.org/10.1016/j.vacuum.2020.109905

[8] Lu Y, Gao X, Jiang L et al (2017) Directly cast bulk eutectic and near-eutectic high entropy alloys with balanced strength and ductility in a wide temperature range. Acta Mater 124:143–150. https://doi.org/10.1016/j.actamat.2016.11.016

[9] Miracle DB, Senkov ON (2017) A critical review of high entropy alloys and related concepts. Acta Mater 122:448–511. https://doi.org/10.1016/j.actamat.2016.08.081

[10] Cantor B, Chang ITH, Knight P, Vincent AJB (2004) Microstructural development in equiatomic multicomponent alloys. Mater Sci Eng A 375–377:213–218. https://doi.org/10.1016/j.msea.2003.10.257

[11] George EP, Curtin WA, Tasan CC (2020) High entropy alloys: a focused review of mechanical properties and deformation mechanisms. Acta Mater 188:435–474. https://doi.org/10.1016/j.actamat.2019.12.015

[12] Lu Y, Dong Y, Jiang H et al (2020) Promising properties and future trend of eutectic high entropy alloys. Scripta Mater 187:202–209. https://doi.org/10.1016/j.scriptamat.2020.06.022

[13] Liu WH, He JY, Huang HL, Wang H, Lu ZP, Liu CT (2015) Effects of Nb additions on the microstructure and mechanical property of CoCrFeNi high-entropy alloys. Intermetallics 60:1–8. https://doi.org/10.1016/j.intermet.2015.01.004

[14] Shun T-T, Chang L-Y, Shiu M-H (2012) Microstructures and mechanical properties of multiprincipal component CoCrFeNiTix alloys. Mater Sci Eng A 556:170–174. https://doi.org/10.1016/j.msea.2012.06.075

[15] Jiang H, Han K, Qiao D, Lu Y, Cao Z, Li T (2018) Effects of Ta addition on the microstructures and mechanical properties of CoCrFeNi high entropy alloy. Mater Chem Phys 210:43–48. https://doi.org/10.1016/j.matchemphys.2017.05.056

[16] Tsai M-H, Fan A-C, Wang H-A (2017) Effect of atomic size difference on the type of major intermetallic phase in arc-melted CoCrFeNiX high-entropy alloys. J Alloys Compd 695:1479–1487. https://doi.org/10.1016/j.jallcom.2016.10.286

[17] Jiang H, Qiao D, Lu Y, Ren Z, Cao Z, Wang T, Li T (2019) Direct solidification of bulk ultrafine-microstructure eutectic high-entropy alloys with outstanding thermal stability. Scripta Mater 165:145–149. https://doi.org/10.1016/j.scriptamat.2019.02.035

[18] Lei Z, Liu X, Wu Y et al (2018) Enhanced strength and ductility in a high-entropy alloy via ordered oxygen complexes. Nature 563(7732):546–550. https://doi.org/10.1038/s41586-018-0685-y

[19] Jodi DE, Park J, Straumal B, Park N (2020) Investigation on the precipitate formation and behavior in nitrogen-containing equiatomic CoCrFeMnNi high-entropy alloy. Mater Lett 258:126806. https://doi.org/10.1016/j.matlet.2019.126806

[20] Li Z (2019) Interstitial equiatomic CoCrFeMnNi high-entropy alloys: carbon content, microstructure, and compositional homogeneity effects on deformation behavior. Acta

Mater 164:400–412. https://doi.org/10.1016/j.actamat.2018.10.050

[21] Wang M, Li Z, Raabe D (2018) In-situ SEM observation of phase transformation and twinning mechanisms in an interstitial high-entropy alloy. Acta Mater 147:236–246. https://doi.org/10.1016/j.actamat.2018.01.036

[22] Stepanov ND, Shaysultanov DG, Chernichenko RS, Yurchenko NY, Zherebtsov SV, Tikhonovsky MA, Salishchev GA (2017) Effect of thermomechanical processing on microstructure and mechanical properties of the carbon-containing CoCrFeNiMn high entropy alloy. J Alloys Compd 693:394–405. https://doi.org/10.1016/j.jallcom.2016.09.208

[23] Wang Z, Baker I, Guo W, Poplawsky JD (2017) The effect of carbon on the microstructures, mechanical properties, and deformation mechanisms of thermo-mechanically treated Fe40.4Ni11.3Mn34.8Al7.5Cr6 high entropy alloys. Acta Mater 126:346–360. https://doi.org/10.1016/j.actamat.2016.12.074

[24] Wu Z, Parish CM, Bei H (2015) Nano-twin mediated plasticity in carbon-containing FeNiCoCrMn high entropy alloys. J Alloys Compd 647:815–822. https://doi.org/10.1016/j.jallcom.2015.05.224

[25] Guo L, Ou X, Ni S, Liu Y, Song M (2019) Effects of carbon on the microstructures and mechanical properties of FeCoCrNiMn high entropy alloys. Mater Sci Eng A 746:356–362. https://doi.org/10.1016/j.msea.2019.01.050

[26] Riva S, Yusenko KV, Lavery NP, Jarvis DJ, Brown SGR (2016) The scandium effect in multicomponent alloys. Int Mater Rev 61(3):203–228. https://doi.org/10.1080/09506608.2015.1137692

[27] Williams JC, Starke EA (2003) Progress in structural materials for aerospace systems11The Golden Jubilee Issue—selected topics in materials science and engineering: past, present and future, edited by S. Suresh. Acta Mater 51(19):5775–5799. https://doi.org/10.1016/j.actamat.2003.08.023

[28] A Standard (2017) Standard test method for microindentation hardness of materials. ASTM International, E384.

[29] Shetty DK, Wright IG, Mincer PN, Clauer AH (1985) Indentation fracture of WC-Co cermets. JMatS 20(5):1873–1882. https://doi.org/10.1007/BF00555296

[30] The measurement of palmqvist toughness for hard and brittle materials (2008) https://www.npl.co.uk/gpgs/measurement-of-palmqvist-toughness.

[31] Palmqvist S (1962) Rißbildungsarbeit bei Vickers-Eindrücken als Maß für die Zähigkeit von Hartmetallen. Archiv für das Eisenhüttenwesen 33(9):629–634. https://doi.org/10.1002/srin.196203379

[32] Muniandy Y, He M, Eizadjou M, George EP, Kruzic JJ, Ringer SP, Gludovatz B (2021) Compositional variations in equiatomic CrMnFeCoNi high-entropy alloys. Mater Charact 180:111437. https://doi.org/10.1016/j.matchar.2021.111437

[33] He JY, Liu WH, Wang H, Wu Y, Liu XJ, Nieh TG, Lu ZP (2014) Effects of Al addition on structural evolution and tensile properties of the FeCoNiCrMn high-entropy alloy system. Acta Mater 62:105–113. https://doi.org/10.1016/j.actamat.2013.09.037

[34] Chen S, Yang X, Dahmen K, Liaw P, Zhang Y (2014) Microstructures and crackling noise of AlxNbTiMoV high entropy alloys. Entropy 16(2):870–884. https://doi.org/10.3390/e16020870

[35] Lin C-M, Juan C-C, Chang C-H, Tsai C-W, Yeh J-W (2015) Effect of Al addition on mechanical properties and microstructure of refractory AlxHfNbTaTiZr alloys. J Alloys Compd 624:100–107. https://doi.org/10.1016/j.jallcom.2014.11.064

[36] Zuo TT, Li RB, Ren XJ, Zhang Y (2014) Effects of Al and Si addition on the structure and properties of CoFeNi equal atomic ratio alloy. J Magn Magn Mater 371:60–68. https://doi.org/10.1016/j.jmmm.2014.07.023

[37] Martins M, Casteletti LC (2009) Sigma phase morphologies in cast and aged super duplex stainless steel. Mater Charact 60(8):792–795. https://doi.org/10.1016/j.matchar.2009.01.005

[38] Juan C-C, Tseng K-K, Hsu W-L et al (2016) Solution strengthening of ductile refractory HfMo x NbTaTiZr high-entropy alloys. Mater Lett 175:284–287. https://doi.org/10.1016/j.matlet.2016.03.133

[39] Yao HW, Qiao JW, Gao MC, Hawk JA, Ma SG, Zhou HF, Zhang Y (2016) NbTaV-(Ti, W) refractory high-entropy alloys: experiments and modeling. Mater Sci Eng A 674:203–211. https://doi.org/10.1016/j.msea.2016.07.102

[40] Poondla N, Srivatsan TS, Patnaik A, Petraroli M (2009) A study of the microstructure and hardness of two titanium alloys: commercially pure and Ti–6Al–4V. J Alloys Compd 486(1):162–167. https://doi.org/10.1016/j.jallcom.2009.06.172

[41] Lopes ESN, Cremasco A, Afonso CRM, Caram R (2011) Effects of double aging heat treatment on the microstructure, Vickers hardness and elastic modulus of Ti–Nb alloys. Mater Charact 62(7):673–680. https://doi.org/10.1016/j.matchar.2011.04.015

[42] Gorsse S, Nguyen MH, Senkov ON, Miracle DB (2018) Database on the mechanical properties of high entropy alloys and complex concentrated alloys. Data Brief 21:2664–2678. https://doi.org/10.1016/j.dib.2018.11.111

[43] Nair RB, Arora HS, Grewal HS (2019) Microwave synthesized complex concentrated alloy coatings: plausible solution to cavitation induced erosion-corrosion. Ultrason Sonochem 50:114–125. https://doi.org/10.1016/j.ultsonch.2018.09.004

[44] Seifi M, Li D, Yong Z, Liaw PK, Lewandowski JJ (2015) Fracture toughness and fatigue crack growth behavior of as-cast high-entropy alloys. JOM 67(10):2288–2295. https://doi.org/10.1007/s11837-015-1563-9

[45] Zhang A, Han J, Su B, Meng J (2018) A promising new high temperature self-lubricating material: CoCrFeNiS0.5 high entropy alloy. Mater Sci Eng A 731:36–43. https://doi.org/10.1016/j.msea.2018.06.030

[46] Hadraba H, Chlup Z, Dlouhy A, Dobes F, Roupcova P, Vilemova M, Matejicek J (2017) Oxide dispersion strengthened CoCrFeNiMn high-entropy alloy. Mater Sci Eng A 689:252–256. https://doi.org/10.1016/j.msea.2017.02.068

[47] Gou Q, Xiong J, Guo Z, Liu J, Yang L, Li X (2021) Influence of NbC additions on microstructure and wear resistance of Ti(C, N)-based cermets bonded by CoCrFeNi high-entropy alloy. Int J Refract Met Hard Mater. https://doi.org/10.1016/j.ijrmhm.2020.105375

[48] Chen F, Gu Y, Xu G, Cui Y, Chang H, Zhou L (2020) Improved fracture toughness by microalloying of Fe in Ti-6Al-4V. Mater Des. https://doi.org/10.1016/j.matdes.2019.108251

[49] Filipovic M, Kamberovic Z, Korac M, Gavrilovski M (2013) Correlation of microstructure with the wear resistance and fracture toughness of white cast iron alloys. Met Mater Int 19(3):473–481. https://doi.org/10.1007/s12540-013-3013-y

[50] Zhang H, He Y, Pan Y (2013) Enhanced hardness and fracture toughness of the laser-solidified FeCoNiCrCuTiMoAlSiB0.5 high-entropy alloy by martensite strengthening. Scripta Mater 69(4):342–345. https://doi.org/10.1016/j.scriptamat.2013.05.020

[51] Putatunda SK, Martis C, Boileau J (2011) Influence of austempering temperature on the mechanical properties of a low carbon low alloy steel. Mater Sci Eng A 528(15):5053–5059. https://doi.org/10.1016/j.msea.2011.03.038

[52] Joseph J, Haghdadi N, Shamlaye K, Hodgson P, Barnett M, Fabijanic D (2019) The sliding wear behaviour of CoCrFeMnNi and AlxCoCrFeNi high entropy alloys at elevated temperatures. Wear 428–429:32–44. https://doi.org/10.1016/j.wear.2019.03.002

[53] Pole M, Sadeghilaridjani M, Shittu J, Ayyagari A, Mukherjee S (2020) High temperature wear behavior of refractory high entropy alloys based on 4–5–6 elemental palette. J Alloys Compd 843:156004. https://doi.org/10.1016/j.jallcom.2020.156004

[54] Deng G, Tieu AK, Su L et al (2020) Investigation into reciprocating dry sliding friction and wear properties of bulk CoCrFeNiMo high entropy alloys fabricated by spark plasma sintering and subsequent cold rolling processes: role of Mo element concentration. Wear 460–461:203440. https://doi.org/10.1016/j.wear.2020.203440

[55] Zhang A, Han J, Su B, Meng J (2017) A novel CoCrFeNi high entropy alloy matrix self-lubricating composite. J Alloys Compd 725:700–710. https://doi.org/10.1016/j.jallcom.2017.07.197

[56] Liu XJ, Yu P, Wang CP, Ishida K (2008) Thermodynamic evaluation of the Co–Sc and Fe–Sc systems. J Alloys Compd 466(1–2):169–175. https://doi.org/10.1016/j.jallcom.2007.11.069

[57] Adhikari P, San S, Zhou C, Sakidja R, Ching W-Y (2019) Electronic structure and mechanical properties of crystalline precipitate phases M23C6(M=Cr, W, Mo, Fe) in Ni-based superalloys. Mater Res Exp 6(11):116323. https://doi.org/10.1088/2053-1591/ab4fb8

[58] Guimarães AA, Mei PR (2004) Precipitation of carbides and sigma phase in AISI type 446 stainless steel under working conditions. J Mater Process Technol 155–156:1681–1689. https://doi.org/10.1016/j.jmatprotec.2004.04.341

[59] Wang W-R, Wang W-L, Wang S-C, Tsai Y-C, Lai C-H, Yeh J-W (2012) Effects of Al addition on the microstructure and mechanical property of AlxCoCrFeNi high-entropy alloys. Intermetallics 26:44–51. https://doi.org/10.1016/j.intermet.2012.03.005

[60] Shi P, Li R, Li Y et al (2021) Hierarchical crack buffering triples ductility in eutectic herringbone high-entropy alloys. Science 373(6557):912–918. https://doi.org/10.1126/science.abf6986

[61] Poletti MG, Fiore G, Gili F, Mangherini D, Battezzati L (2017) Development of a new high entropy alloy for wear resistance: FeCoCrNiW0.3 and FeCoCrNiW0.3+ 5 at.% of C. Mater Des 115:247–254. https://doi.org/10.1016/j.matdes.2016.11.027

[62] Kwon H, Moon J, Bae JW et al (2020) Precipitation-driven metastability engineering of carbon-doped CoCrFeNiMo medium-entropy alloys at cryogenic temperature. Scripta Mater 188:140–145. https://doi.org/10.1016/j.scriptamat.2020.07.023

[63] Christofidou KA, Pickering EJ, Orsatti P, Mignanelli PM, Slater TJA, Stone HJ, Jones NG (2018) On the influence of Mn on the phase stability of the CrMnxFeCoNi high entropy alloys. Intermetallics 92:84–92. https://doi.org/10.1016/j.intermet.2017.09.011

[64] Campbell K, Honeycombe RWK (1974) The isothermal decomposition of austenite in simple chromium steels. Metal Sci 8(1):197–203. https://doi.org/10.1080/03063453.1974.11910766